How to cite: *Angew. Chem. Int. Ed.* **2025**, *64*, e202504499
doi.org/10.1002/anie.202504499

**Electrochemistry** **Very Important Paper**

# Mechanistic Insights into the $CO_2$-Assisted NO Electrochemical Deoxygenation and Hydrogenation

*Pan Li*[+], *Yi Liu*[+], *Liangyiqun Xie, Guangtao Wang, Xuanzhao Lu, Jian Li, Xuanhao Wu, Yujing Jiang, and Wenlei Zhu**

**Abstract:** Electrocatalytic NO reduction to $NH_3$ holds significant potential for pollutant treatment and resource recovery. Herein, we report that the introduction of $CO_2$ on octahedral oxide-derived copper (o-OD-Cu) significantly enhances the electrochemical reduction of NO to $NH_3$. With 10% NO in a $CO_2$ environment, the Faradaic efficiency for $NH_3$ production in a flow cell remains around 80% over a wide current density range from 20 to 250 mA $cm^{-2}$. At a current density of 250 mA $cm^{-2}$, the yield can reach up to 1403.9 μmol $cm^{-2}$ $h^{-1}$, which is 3.71 times higher than without $CO_2$ and surpasses the performance reported in similar literature. Moreover, even at a low concentration of 1% NO, the Faradaic efficiency can reach a maximum of 70.11% at a current density of 20 mA $cm^{-2}$. In situ investigations and theoretical calculations revealed that, in the coexistence of NO and $CO_2$, the NO reduction pathway involves a unique route wherein *CO and *COOH, produced from $CO_2$ reduction, can respectively promote the deoxygenation of *NO and hydrogenation of *N by acquiring O atoms from *NO and providing H atoms for the sustained hydrogenation of *N, thereby accelerating the conversion process of NO to $NH_3$.

## Introduction

Ammonia ($NH_3$) plays a significant role in both agricultural and industrial production, with an annual output exceeding 200 million tons.[1–4] Due to its high gravimetric hydrogen density, $NH_3$ is also considered a clean energy carrier for chemical energy storage applications and is anticipated to become a low-carbon energy vector in the future.[5,6] Currently, the Haber–Bosch process, the predominant method for industrial $NH_3$ synthesis, operates under high-temperature and high-pressure conditions, relies on fossil fuels, and uses $N_2$ and $H_2$ as the primary reactants.[1,7] The production of $NH_3$ can account for 20% of the energy consumption and 35% of the $CO_2$ emissions in the chemical industry, highlighting the significant environmental impact of $NH_3$ synthesis via the Haber–Bosch process.[8,9] With the advancement of clean electrical energy, the electrochemical synthesis of $NH_3$ from $N_2$ represents a promising alternative to traditional methods.[10,11] Nonetheless, the industrial application of electrochemical $N_2$ reduction faces several challenges, including the high dissociation energy of the N≡N bond (941 kJ $mol^{-1}$), low solubility of $N_2$ in electrolytes, and competition with the hydrogen evolution reaction, resulting in suboptimal $NH_3$ Faradaic efficiencies and reaction rates.[12–15]

Nitric oxide (NO) is a major atmospheric pollutant, mainly originating from industrial emissions, vehicle exhausts, and power generation.[16,17] It contributes to severe environmental issues such as photochemical smog, acid rain, and ozone depletion, posing significant threats to human health and ecological systems.[16,18,19] Selective catalytic reduction (SCR) is a widely used technique for NO abatement, typically employing catalysts to convert NO into harmless $N_2$ using $NH_3$ or $H_2$ as reductants under high-temperature conditions.[20,21] However, this method is associated with high operational costs and the potential for secondary pollution.[22–24] Therefore, the electrochemical conversion of harmful NO into economically valuable $NH_3$ has emerged as a promising strategy, attracting increasing attention in recent years.[2,16,22,23,25–28] Research indicates that electrocatalytic NO reduction to produce $NH_3$ can achieve a high $NH_3$ selectivity (Faradaic efficiency > 95%), with almost no by-products generated during the reaction. Notably, some systems can maintain high selectivity while achieving industrial-level current densities exceeding 200 mA $cm^{-2}$, demonstrating significant potential for practical application.[29–31] However, as far as we know, most current studies on electrocatalytic NO reduction reaction use pure NO or Ar-diluted NO feed, without considering the role of other gas components in flue gas (Table S1). Since NO is produced by the combustion of fossil fuels, its concentration is generally low.[25,28] Consequently, various gas components inevitably coexist with NO in flue gas, such as $N_2$, $CO_2$, CO, and others. Additionally, some notable research has reported that the introduction of gas molecules

[*] P. Li[+], Y. Liu[+], L. Xie, G. Wang, X. Lu, J. Li, Y. Jiang, W. Zhu
State Key Laboratory of Pollution Control and Resource Reuse, State Key Laboratory of Analytical Chemistry for Life Science, School of Environment, School of Chemistry and Chemical Engineering, Nanjing University, Nanjing 210023, China
E-mail: wenleizhu@nju.edu.cn

X. Wu
Department of Environmental Engineering, Zhejiang Provincial Engineering Research Center of Industrial Boiler & Furnace Flue Gas Pollution Control, Zhejiang University, Hangzhou 310058, China

[+] Both authors contributed equally to this work.

Additional supporting information can be found online in the Supporting Information section

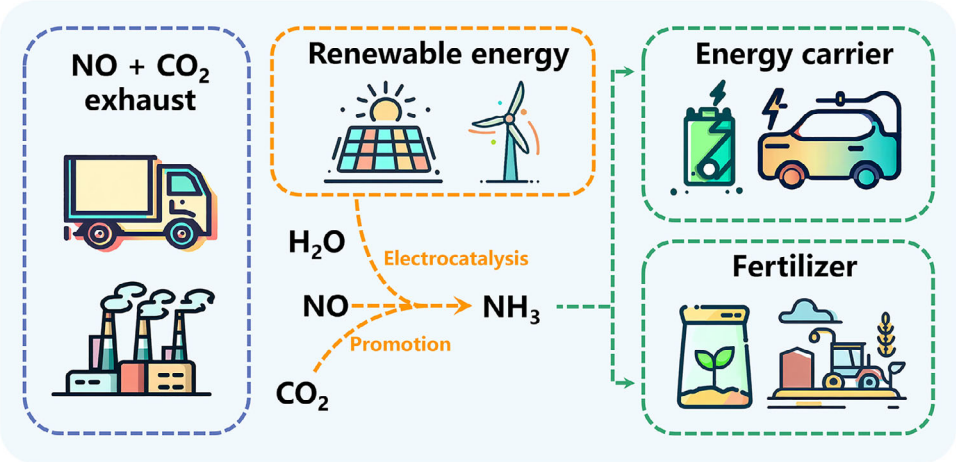


***Scheme 1.*** Schematic diagram of $CO_2$-promoted NO electrochemical reduction to $NH_3$. Low-concentration nitrogen sources (NO) are derived from vehicle or factory exhaust gases. Electrical energy for the process can be generated from renewable sources such as solar or wind energy. The produced ammonia can serve as a chemical energy carrier and as a raw material for fertilizers.

(such as $CO_2$) or their derivatives can enhance the original electrocatalytic reaction rates and selectivity, including the electrocatalytic reduction of chlorinated hydrocarbons and nitrites, as well as the electrocatalytic oxidation of water.[32–34] Therefore, to promote the industrial application of electrocatalytic NO reduction to produce $NH_3$, it is necessary to systematically study the effects of different gas components on electrocatalytic NO reduction.

In recent years, significant research efforts have been devoted to investigating precious metals and transition metal-based catalysts for NO electrocatalytic reduction.[2,16,25,26,31,35–39] However, the catalytic performance of these materials is limited by the adsorption characteristics of key intermediates. Metals such as Ag, Au, and In exhibit weak adsorption abilities for *NO, resulting in the ineffective activation of NO molecules on their surfaces. Although Pt, Pd, and Ni systems possess moderate *NO adsorption energies, their strong *H adsorption characteristics induce vigorous hydrogen evolution reactions, thereby significantly reducing Faradaic efficiency. In contrast, Cu-based catalysts achieve moderate *NO adsorption while maintaining weak *H adsorption strength, demonstrating excellent NO catalytic activity.[16,31,40] Combined with their significant cost-effectiveness, Cu-based catalysts emerge as ideal candidates for industrial-scale electrochemical NO reduction. Moreover, Cu-based catalysts, due to their unique *CO binding capabilities and the absence of under potential deposited hydrogen ($H_{upd}$), exhibit excellent performance in the electrocatalytic reduction of both $CO_2$ and CO, representing the sole class of metals capable of directly converting $CO_2$ and CO into high-selectivity, valuable oxygenates and hydrocarbons.[41–46]

Herein, we propose a strategy based on Cu-based catalysts to enhance the electroreduction of NO to $NH_3$ by introducing $CO_2$ (Scheme 1). The synergistic effect of $CO_2$ and Cu-based catalysts extends the catalytic process beyond traditional electrocatalysis on the electrode surface. The introduction of gaseous $CO_2$ creates a broader catalytic interface, thereby enhancing catalytic efficiency and selectivity. According to previous literature, the Cu(111) surface is an effective interface for the electrocatalytic reduction of NO to $NH_3$.[16,47] Therefore, octahedral oxide-derived copper (o-OD-Cu) was prepared from octahedral $Cu_2O$ (o-$Cu_2O$) with (111) facets.[48] Additionally, c-OD-Cu and t-OD-Cu, derived from cubic $Cu_2O$ (c-$Cu_2O$) with (100) facets and truncated octahedral $Cu_2O$ (t-$Cu_2O$) containing both (100) and (111) facets, respectively, were also prepared as controls. We first investigated the effects of gaseous components ($N_2$, $CO_2$, CO) in flue gas on the electrocatalytic reduction of NO. Interestingly, the presence of $CO_2$ can significantly enhance the performance of OD-Cu in the reduction of NO to $NH_3$, and it was found that the Cu(111) facet has a more favorable effect on $NH_3$ production compared to the Cu(100) facet in the presence of $CO_2$. The highest $NH_3$ yield can reach 1403.9 μmol $cm^{-2}$ $h^{-1}$, which is far superior to the reduction performance reported in the literature for NO at the same concentration. Even at low NO concentrations in simulated flue gas, the $NH_3$ production performance is better than that reported in other studies on low-concentration NO. In situ Raman spectroscopy, in situ infrared spectroscopy, and theoretical calculations indicate that *CO and *COOH adsorbed on the surface of Cu catalysts can, respectively, promote the deoxygenation process of *NO and the hydrogenation process of *N, thereby assisting the electroreduction of NO to $NH_3$.

## Results and Discussion

$Cu_2O$ particles exhibiting three distinct morphologies—octahedral (o-$Cu_2O$), truncated octahedral (t-$Cu_2O$), and cubic (c-$Cu_2O$)—were prepared using a slightly modified method.[48,49] Figure S1 displays the X-ray diffraction (XRD) pattern of the prepared $Cu_2O$ particles. The distinct peaks at $2\theta$ values of 36.5°, 42.4°, 61.6°, and 73.7° are indicative of the (111), (200), (220), and (311) crystalline planes of $Cu_2O$, as indexed in the JCPDS file 01-77-0199. The X-ray

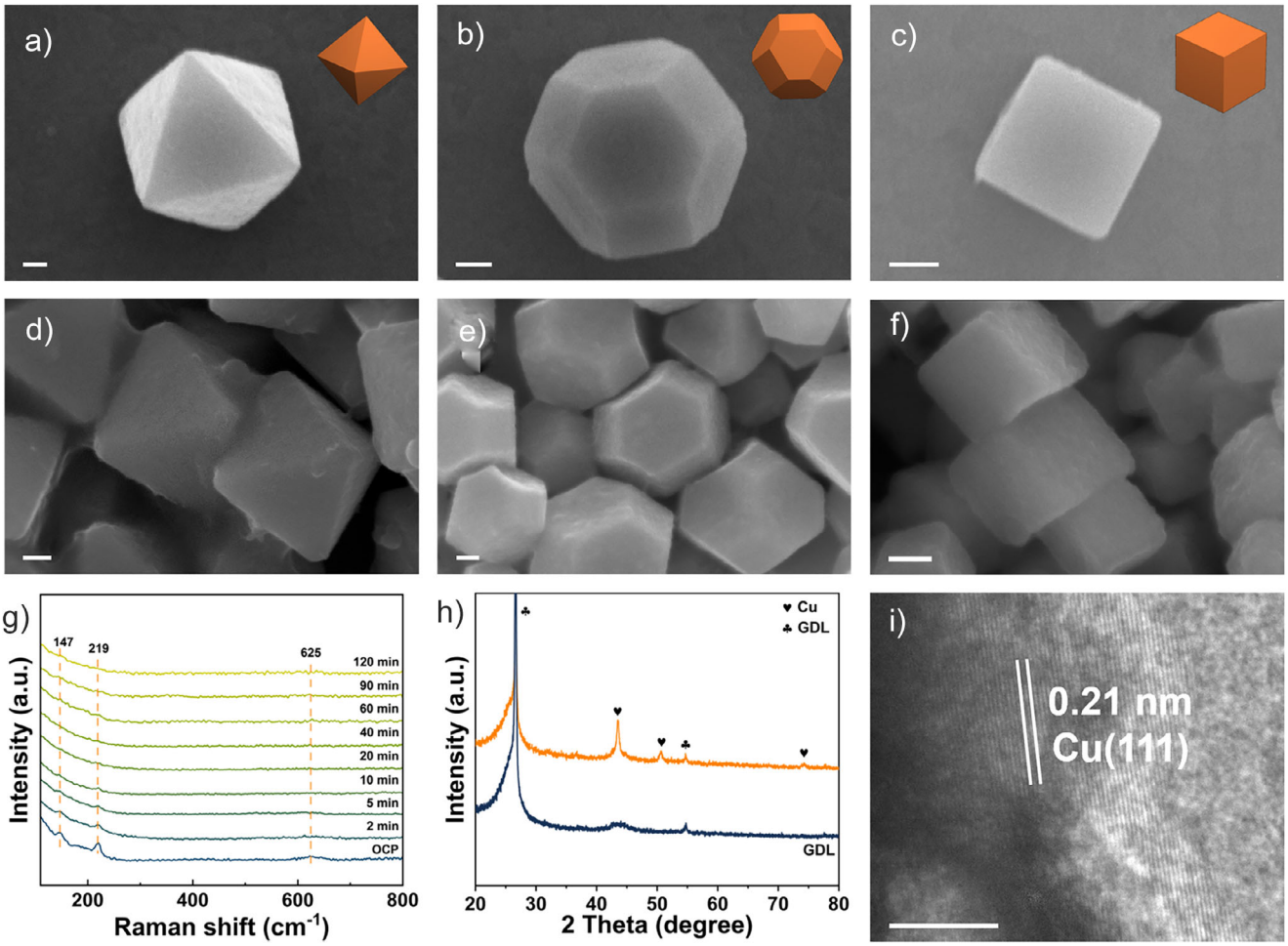


***Figure 1.*** Morphologies and structural characterization. SEM images of a,d) o-$Cu_2O$, b,e) t-$Cu_2O$, and c,f) c-$Cu_2O$ a–c) before and d–f) after pre-reduction treatment. Scale bar, 200 nm a–f). g) In situ Raman spectra of o-$Cu_2O$ during pre-reduction. h) XRD patterns of o-$Cu_2O$ after pre-reduction treatment. i) HRTEM images of o-$Cu_2O$ after pre-reduction treatment. Scale bar, 5 nm i).

photoelectron spectroscopy (XPS) also confirms the exclusive presence of peaks corresponding to $Cu_2O$ in the samples, consistent with the XRD results (Figure S2). Scanning electron microscopy (SEM) images demonstrate that the geometric shapes of particles can be finely tuned by modulating the concentration of polyvinylpyrrolidone (PVP) (Figure 1a–c). As illustrated in Figures S3–S7, the broad views of SEM and transmission electron microscopy (TEM) images further corroborate the uniformity of the synthesized $Cu_2O$ particles.

Due to the relatively low reduction potential of $Cu_2O$, maintaining stability under reductive environments is challenging. Therefore, prior to the electrocatalytic reaction, the gas diffusion electrode (GDE) coated with $Cu_2O$ was subjected to a pre-reduction treatment. SEM images show that, except for the surface becoming rough, the particles after pre-reduction still retain their original morphology (Figure 1d–f). To further investigate the dynamic evolution of $Cu_2O$ under prolonged reductive potential, in situ Raman spectroscopy was performed on o-$Cu_2O$ in a commercial Raman electrochemical cell. The in situ Raman spectra, as shown in Figure 1g, reveal that the characteristic Raman peaks of $Cu_2O$ (147, 219, and 625 $cm^{-1}$, consistent with the Raman spectra under non-in situ conditions, as shown in Figure S8) gradually diminish and nearly vanished after 20 min under reductive potential conditions. The result indicates that $Cu_2O$ transforms into metallic Cu under reduction conditions, consistent with the XRD analysis (Figure 1h). High-resolution transmission electron microscopy (HRTEM) images further show that after pre-reduction of $Cu_2O$ with three different morphologies, crystal lattice fringes belonging to the (111) or (100) plane of metallic Cu are clearly visible (Figure 1i, Figures S9, and S10).

The impact of different gas components on the electrocatalytic reduction of NO to $NH_3$ was investigated using a flow cell. The structure and composition of the flow cell, as shown in Figure 2a, includes independent gas and electrolyte chambers, separated by a GDE coated with $Cu_2O$ (Figure S11). This configuration effectively isolates the gas from the electrolyte, facilitating the construction of a stable gas-catalyst-electrolyte interface while circumventing the mass transfer limitations due to the low solubility of NO (Figure 2b). After the pre-electroreduction treatment of the GDE coated with o-$Cu_2O$, NO was mixed with common gas components from flue gas ($N_2$, $CO_2$, CO) separately and introduced into a flow

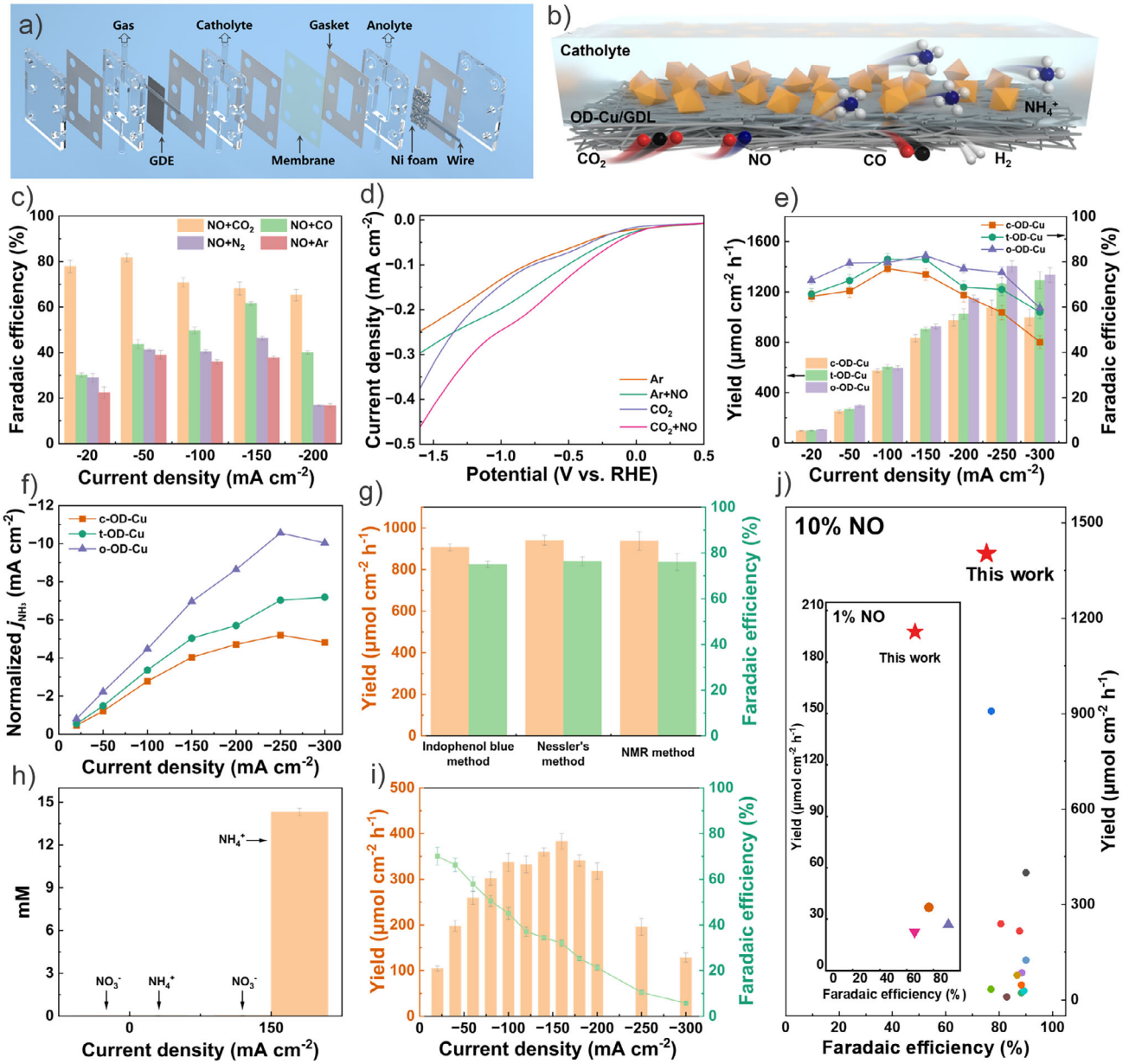


***Figure 2.*** Study on the performance of electrocatalytic reduction of NO to $NH_3$. a) Illustration of the flow cell design and components. b) Enlarged schematic showing the detailed interaction at the gas-catalyst–electrolyte interface. c) Faradaic efficiency of electrocatalytic $NH_3$ synthesis from NO under different atmospheres. d) Linear sweep voltammetry (LSV) of o-OD-Cu under different atmospheres. e) Yield and Faradaic efficiency of $NH_3$ on c-OD-Cu, t-OD-Cu, and o-OD-Cu tested with $CO_2$ at various currents in 1 M $KHCO_3$ electrolyte. f) ECSA normalized $NH_3$ partial current density for c-OD-Cu, t-OD-Cu, and o-OD-Cu. g) Yield and Faradaic efficiency of $NH_3$ determined by the indophenol blue, Nessler's reagent method, and NMR method. h) Concentrations of $NO_3^-$ and $NH_4^+$ in the electrolyte at a current density of 150 mA $cm^{-2}$ and without electrolysis. i) Yield and Faradaic efficiency of $NH_3$ electroreduction in 1% NO/$CO_2$. j) Comparative performance of o-OD-Cu in NO electroreduction against reported catalysts (see detailed information in Table S1).

cell to investigate the impact of different gases on the electrocatalytic reduction of NO to produce $NH_3$. As a control, the inert gas Ar was mixed with NO. The volume concentration of NO after mixing with different gas components was 10% (unless otherwise stated, the default concentration of NO is 10%). $NH_3$ produced in the electrolyte was quantified using the indophenol blue method (Figure S12).

According to Figure 2c, the electrocatalytic reduction performance of NO to $NH_3$ in a $N_2$ atmosphere is comparable to that in the control group with Ar, and may even be slightly better. This could be due to a small amount of $N_2$ participating in the electrocatalytic reaction and being reduced to $NH_3$. Surprisingly, the reduction performance of NO to $NH_3$ in the presence of $CO_2$ and CO is superior to that in $N_2$ and Ar atmospheres. Although both $CO_2$ and CO can facilitate the reduction of NO to $NH_3$, $CO_2$ has a more pronounced effect, enhancing the performance of the electrocatalytic reduction of NO across a broad range of

current densities (20–200 mA $cm^{-2}$). At current densities of 20 and 50 mA $cm^{-2}$, the presence of CO shows almost no improvement in the performance of NO reduction to $NH_3$. Even at 100 to 200 mA $cm^{-2}$, although the presence of CO results in some performance improvement compared to that in $N_2$ and Ar atmospheres, the enhancement is still less pronounced than with $CO_2$. Figure 2d depicts the LSV results of o-OD-Cu under various gas atmospheres. The results indicate that, under pure $CO_2$ atmosphere, the current density for o-OD-Cu is higher than that under pure Ar atmosphere, suggesting that $CO_2$ electroreduction reaction occurs. The introduction of NO, regardless of whether it is in an Ar or $CO_2$ atmosphere, significantly increases the current density, indicating that NO electrocatalytic reaction is taking place. It is particularly noteworthy that, despite both having a 10% NO concentration, the current density in a $CO_2$ atmosphere is substantially higher compared to that in an Ar atmosphere. Similar phenomena were observed on both c-OD-Cu and t-OD-Cu, where the current density for NO and $CO_2$ is higher than for pure $CO_2$, indicating that NO is more readily reduced than $CO_2$ (Figure S13).

To further investigate the impact of three different morphologies of OD-Cu on the NO reduction performance in a $CO_2$ atmosphere, the experiment initially employed the flow cell with 0.2 M $KHCO_3$ as the electrolyte. Electrochemical tests were conducted at different current densities to evaluate the yield and Faradaic efficiency of electrocatalytic reduction of NO to $NH_3$. Figure S14 indicates that, under the condition of NO and $CO_2$ as the feed gas, the three different morphologies of OD-Cu exhibit comparable $NH_3$ yield and Faradaic efficiency. Among them, o-OD-Cu demonstrates slightly better performance in the electrocatalytic reduction of NO to $NH_3$. Under the same conditions, it was found that using 1 M $KHCO_3$ as the electrolyte could obtain higher $NH_3$ yield and Faradaic efficiency compared to 0.2 M $KHCO_3$ (Figure 2e). In 1 M $KHCO_3$ electrolyte, o-OD-Cu shows slightly better performance than c-OD-Cu and t-OD-Cu in electrocatalytic reduction of NO to $NH_3$, consistent with the results obtained using 0.2 M $KHCO_3$ as the electrolyte. At a current density of 150 mA $cm^{-2}$ the Faradaic efficiency of $NH_3$ reaches a maximum of 82.73%, with a corresponding yield of 926.0 µmol $cm^{-2}$ $h^{-1}$. When the current density is increased to 250 mA $cm^{-2}$, although there is a slight decrease in Faradaic efficiency, it still maintains at 75.25%, while the yield increases to its highest value of 1403.9 µmol $cm^{-2}$ $h^{-1}$. Additionally, the performance of o-OD-Cu for NO reduction in an Ar atmosphere with 1 M $KHCO_3$ as the electrolyte was tested (Figure S15). The results indicated that, consistent with previous observations, the $NH_3$ production performance is inferior to that in a $CO_2$ atmosphere, particularly at higher current densities, where the Faradaic efficiency significantly decreases. At a current density of 250 mA $cm^{-2}$, the $NH_3$ production performance under $CO_2$ conditions is 3.71 times higher than that under Ar conditions.

Moreover, the hydrogen evolution reaction (HER) as a competing process during NO electroreduction was examined in both $CO_2$ and Ar environments (Figures S16 and S17). At low current densities, the volume of $H_2$ evolved remained negligible in both atmospheres, suggesting preferential NO reduction over HER.[50] Notably, under high current density conditions, the $CO_2$ atmosphere exhibited a lower hydrogen production compared to the Ar atmosphere. This suggests that the presence of $CO_2$ enhances the hydrogenation of nitrogen-containing intermediates during NO electroreduction, thereby suppressing the competing HER. To investigate the impact of different morphologies of OD-Cu on the electrochemical enhancement of $CO_2$ for the reduction of NO to $NH_3$, the electrochemical active surface area (ECSA) of three different morphologies of catalysts was first evaluated. Cyclic voltammetry curves were obtained at different scan rates with a potential window where no Faradaic reactions occur (Figure S18 and Table S2). From these curves, the double-layer capacitance ($C_{dl}$) and roughness factor were calculated. A comparison of the $NH_3$ partial current, normalized by ECSA, revealed that the activity of o-OD-Cu is higher than that of c-OD-Cu and t-OD-Cu (Figure 2f). This suggests that the Cu(111) facet may exhibit superior catalytic activity for the reduction of NO to $NH_3$ in the presence of $CO_2$ compared to the Cu(100) facet.

In the cycle experiments under different gas conditions, it was found that the Faradaic efficiency of $NH_3$ produced by NO in a $CO_2$ atmosphere is significantly higher than that in an Ar atmosphere (Figure S19). Furthermore, the absence of NO resulted in no $NH_3$ production, indirectly confirming that $NH_3$ originates from the conversion of NO. In addition, the liquid products from the electrocatalytic reduction of pure $CO_2$ and pure CO were analyzed using $^1H$ NMR, revealing several carbon-related products such as formic acid, acetic acid, ethanol, and propanol. The concentrations of these products generally increased with the rise in current density (Figure S20a,b). However, when introducing NO in a $CO_2$ or CO atmosphere, even at high current densities, the resulting electrolyte solution contained almost no carbon-related products (Figure S20c,d). This is likely because NO is more easily reduced than $CO_2$ and CO, consistent with the previously mentioned LSV analysis results. The indophenol blue method was simultaneously used to test the electrolyte solutions after the reduction of pure $CO_2$ at different currents. It was noted that the absorbance of the carbon-related liquid products under each current showed no difference compared to the blank control, indicating that the liquid products of $CO_2$ reduction have almost no impact on the indophenol blue method (Figure S21). In addition, Nessler's reagent and NMR spectroscopy were both utilized to further quantify the concentration of $NH_3$ in the products. The results were found to be consistent with those obtained using the indophenol blue method, confirming the reliability of the $NH_3$ test results (Figure 2g, Figures S22 and S23).

Given NO and $O_2$ readily react to form $NO_2$, which is highly soluble in water and subsequently transforms into $NO_3^-$, it is important to investigate whether the source of the electroreduction to $NH_3$ is the direct electrocatalysis of NO or the electrocatalysis of $NO_3^-$ converted from NO.[23] A colorimetric method was used to measure $NO_3^-$ concentration in the electrolyte solution (Figure 2h and Figure S24). As shown in Figure 2h, before electrolysis, the electrolyte solution contained neither $NO_3^-$ nor $NH_4^+$. Upon reaching a current density of 150 mA $cm^{-2}$, $NO_3^-$ concentration was observed

to be nearly negligible, whereas a significant amount of $NH_4^+$ was generated. These observations indicate that $NH_4^+$ is formed via direct electrocatalytic reduction of NO. Previous literature has reported the electrocatalytic synthesis of urea when NO and $CO_2$ are used as feed gases.[51] Therefore, the concentration of urea in the electrolyte solution was also measured using the diacetylmonoxime method. The results indicated that urea production was negligible, with almost no urea detected (Figures S25 and S26).

In the actual flue gas, the concentration of NO is quite low, therefore, 1% concentration of NO is introduced as the feed gas in a $CO_2$ atmosphere (1% NO/$CO_2$).[25,28,52–54] Under this condition, it was observed that the Faradaic efficiency decreases with the increase in current density due to the mass transfer limitation of NO. However, at current densities of 20 and 40 mA $cm^{-2}$, the Faradaic efficiencies can reach 70.11% and 66.26%, corresponding to $NH_3$ yields of 104.6 and 197.8 μmol $cm^{-2}$ $h^{-1}$, respectively (Figure 2i). The long-term stability of o-OD-Cu in 1% NO/$CO_2$ for electrocatalytic $NH_3$ synthesis has been tested. During this period, portions of electrolyte were periodically extracted to quantitatively measure the concentration of $NH_3$. Figure S27 shows that within 10 h of operation, the Faradaic efficiency of $NH_3$ could be maintained at around 70%, with no significant increase in overpotentials. XRD and Auger electron spectroscopy analyses of the post-reaction electrode revealed that it remained nearly in the metallic Cu state, with only a small portion oxidized due to air exposure (Figure S28). This is consistent with the results after pre-electrolysis, indicating that the catalyst exhibits good stability. By introducing $CO_2$, the $NH_3$ yield from the electroreduction of NO is significantly higher than the results reported in the literature, both at 10% NO concentration and at the lower 1% NO concentration levels (Figure 2j and Table S1). Moreover, the Faradaic efficiency remains stable over a wide range of current densities.

Furthermore, the effect of different electrolytes on the $CO_2$ enhancement performance was investigated in the process of reducing NO to $NH_3$ using o-OD-Cu as a catalyst. Under the same experimental conditions, when the weakly basic $KHCO_3$ electrolyte was replaced with the neutral $Na_2SO_4$ and the basic KOH, NO reduction experiments were conducted in NO/Ar and NO/$CO_2$ environments. The study found that in the $Na_2SO_4$ electrolyte, the presence of $CO_2$ significantly promoted the electrocatalytic reduction of NO to produce $NH_3$, similar to the effect observed in $KHCO_3$ electrolyte (Figure S29). However, whether under NO/Ar or NO/$CO_2$ conditions, the performance of $Na_2SO_4$ as an electrolyte is not as good as that of $KHCO_3$, possibly due to the presence of $KHCO_3$ causing a slightly higher concentration of $CO_2$ near the active sites compared to $Na_2SO_4$.[55] In the KOH electrolyte, regardless of the presence of $CO_2$, the Faradaic efficiency for $NH_3$ was relatively low, which may be related to the unsuitable pH value (Figure S30). However, at lower current densities, the presence of $CO_2$ could still improve the Faradaic efficiency for $NH_3$ and maintain this efficiency over a wider range of current densities. Therefore, this further confirms that $CO_2$ can enhance the performance of electrocatalytic reduction of NO to $NH_3$. This effect transcends the confines of particular electrolytes, establishing that $HCO_3^-$ is not a key factor promoting the reduction of NO, but rather the presence of $CO_2$ molecules facilitates the reduction of NO. Moreover, using commercial silver (Ag) powder as the catalyst under the same conditions, the results showed that at higher current densities, the presence of $CO_2$ could still enhance the Faradaic efficiency for $NH_3$ and maintain a higher efficiency over a wide current density range (Figure S31). However, the Faradaic efficiency of Ag is far less than that of Cu-based catalysts under the same condition, suggesting that Cu-based catalysts may work synergistically with $CO_2$ to better facilitate the reduction of NO to $NH_3$. Therefore, it was speculated that $CO_2$ can enhance the efficiency of copper-based catalysts in reducing NO to $NH_3$, possibly because the adsorption of $CO_2$ molecules or their intermediates during the reduction process on the surface of copper-based catalysts synergistically promotes the reduction of NO.

To verify this hypothesis, in situ Raman spectroscopy was used to study the variation of reaction intermediates on the surface of o-OD-Cu under the conditions of NO/$CO_2$, NO/Ar, and pure $CO_2$ atmospheres (Figure 3a–c). Under NO/Ar conditions, the adsorption peak of *NO was observed at 1350 $cm^{-1}$, the peak of *NH at 1566 $cm^{-1}$, and the peak of *$NH_3$ at 1591 $cm^{-1}$.[56–59] Conversely, under NO/$CO_2$ conditions, these corresponding peaks were not observed, possibly due to the presence of $CO_2$ accelerating the desorption process of *NH and *$NH_3$. In the presence of $CO_2$ alone, weaker *CO peaks were observed at 2045 and 2085 $cm^{-1}$.[48,60] Notably, under NO/$CO_2$ conditions, the *CO peaks appeared much stronger, indicating that a significant amount of *CO had been adsorbed on the surface of the catalyst. These adsorbed *CO may facilitate the deoxygenation process of NO and the protonation process of *N. In the CO-SCR reaction, CO participates by reducing NO to $N_2$ while being oxidized to $CO_2$.[61–63] Does this suggest that a similar process might occur during the electrochemical reduction, where *CO interacts with *NO? Therefore, it is hypothesized that during the electrocatalytic process, *CO produced from the reduction of $CO_2$ may reacquire an O atom and revert to $CO_2$, thereby facilitating the deoxygenation reaction of *NO. To verify that *CO can facilitate the deoxygenation of NO to produce $CO_2$, electrocatalytic tests were conducted under NO/CO conditions, and the exhaust was absorbed using a clarified BaOH solution. To eliminate the interference of $CO_2$ impurities, a wash bottle containing 3 M NaOH was used during gas intake, and the electrolyte was replaced with 1 M $Na_2SO_4$. After the reaction had proceeded for 5 h, the $Ba(OH)_2$ solution turned white and turbid. The white precipitates were confirmed to be $BaCO_3$ through XRD analysis, indicating that $CO_2$ was indeed generated during the electrochemical reduction process under the coexistence of NO and CO (Figure S32). This demonstrates that *CO can facilitate the deoxygenation process during the electrochemical reduction of NO.

Although Figure 2c shows that the presence of CO can enhance the reduction of NO to $NH_3$, the degree of enhancement is less significant than that of $CO_2$. Does this suggest that there are other intermediates facilitating the reduction of NO to $NH_3$? It is therefore hypothesized that while *CO can indeed assist in the deoxygenation

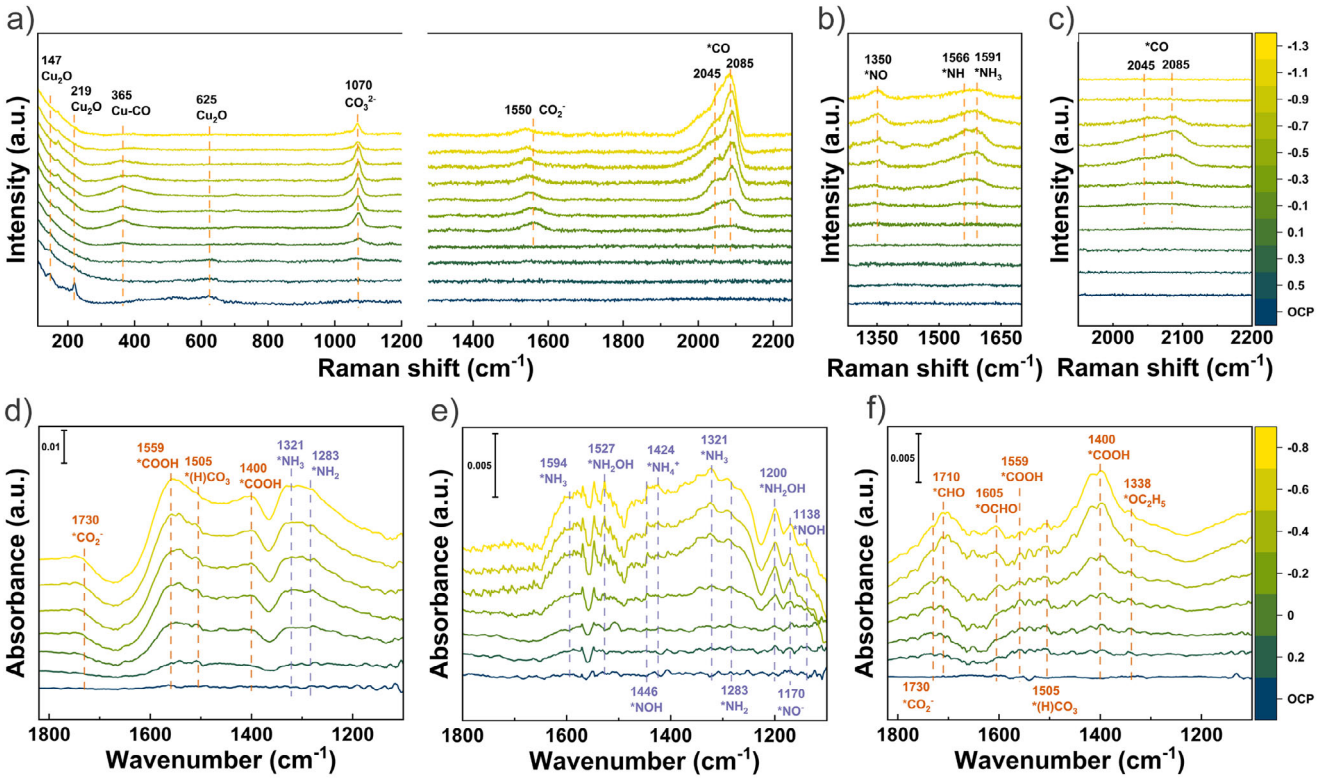


***Figure 3.*** In situ characterization. a–c) In situ Raman spectra and d–f) in situ FTIR spectra of o-OD-Cu under varying applied potentials in the presence of a,d) NO and $CO_2$, b,e) NO and Ar, and c,f) $CO_2$.

process of NO, other carbon-related intermediates formed during the reduction of $CO_2$ facilitate the hydrogenation of NO, and these intermediates are not produced during the reduction of CO. To further supplement and validate the aforementioned findings, as well as elucidate the reaction pathway of $CO_2$ in promoting the electrocatalytic reduction of NO to $NH_3$, in situ Fourier transform infrared spectroscopy (FTIR) was employed to monitor the intermediates formed during the electrochemical catalysis under three different gas conditions (Figure 3d-f). Under the conditions of Ar and NO, the spectra reveal a series of intermediate peaks related to NO reduction, including $*NO^-$, *NOH, $*NH_2OH$, $*NH_2$, and $*NH_3$ (Figure 3e).[39,47,64–68] This confirms that in the absence of $CO_2$, the NO reduction pathway follows $*NO \rightarrow *NOH \rightarrow *N \rightarrow *NH \rightarrow *NH_2 \rightarrow *NH_3$ (Figure S33).[16,47] In addition, the presence of $*NH_2OH$ suggests that $NH_2OH$ might form during NO reduction under Ar atmosphere. The detection of $NH_2OH$ in the electrocatalytic NO reduction products under Ar atmosphere further validates this observation (Figures S34 and S35). Although the Faradaic efficiency of $NH_2OH$ was low at high current densities, it showed significantly higher values at lower current densities, demonstrating the existence of a by-product formation pathway during NO electroreduction under NO/Ar coexisting conditions. The reaction mechanism likely follows the pathway $*NO \rightarrow *NOH \rightarrow *NHOH \rightarrow *NH_2OH$.[47,50] However, in the presence of both $CO_2$ and NO, only the characteristic peaks of $NH_2$ and $NH_3$ were observed, while the peaks of *NO, *NOH, and $NH_2OH$ disappeared (Figure 3d). This phenomenon indicates that the presence of $CO_2$ significantly alters the pathway of NO reduction, further confirming that *CO can promote the deoxygenation process of NO. Specifically, *CO produced by the reduction of $CO_2$ reacquires an oxygen atom and is reduced back to $CO_2$, resulting in the direct conversion of *NO to *N, bypassing the $*NO \rightarrow *NOH \rightarrow *N$ pathway.

In the spectra of the reaction system with pure $CO_2$, multiple characteristic vibration peaks of carbon-related intermediates were observed (Figure 3f). The characteristic peak at 1720 $cm^{-1}$ is attributed to the $*CO_2^-$, which can capture protons and convert into *COOH, a key intermediate for the formation of *CO.[69–71] The vibrational signal at 1710 $cm^{-1}$ corresponds to the *CHO, which is formed due to the further protonation of *CO.[72,73] Additionally, the characteristic peak at 1605 $cm^{-1}$ indicates the presence of the *OCHO, a characteristic intermediate in the HCOOH formation pathway.[70,74] The vibrational peak at 1338 $cm^{-1}$ can be attributed to the $*OC_2H_5$, an intermediate for the formation of $C_2H_5OH$. These phenomena are consistent with previous NMR data, showing that HCOOH and $C_2H_5OH$ are produced only during the reduction of $CO_2$ alone, whereas they are hardly generated under the co-electrolysis conditions of NO and $CO_2$ (Figure S20). This indicates that the presence of NO hinders certain pathways in the $CO_2$ reduction process. In the spectra under the coexistence of $CO_2$ and NO, only $*CO_2^-$ and *COOH were observed, with a stronger peak for *COOH (Figure 3d). Moreover, *COOH is produced by the reduction of $CO_2$ and not by the reduction of CO,

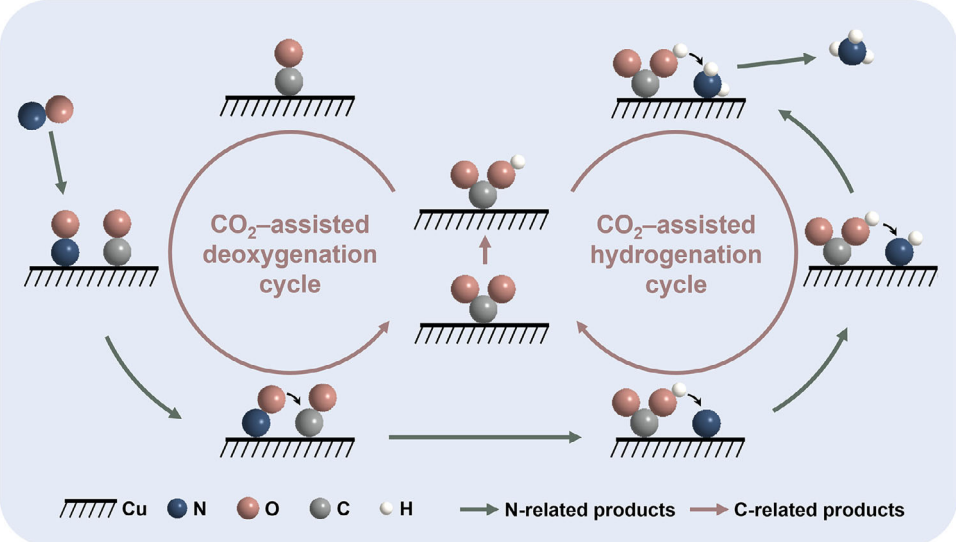


***Scheme 2.*** Reaction pathway for the electrochemical reduction of NO to $NH_3$ promoted by $CO_2$.

suggesting that these adsorbed *COOH species may assist the subsequent hydrogenation of *N in the NO reduction process. This explains why $CO_2$ promotes the reduction of NO to $NH_3$ more effectively than CO.

Based on the experimental results, a mechanism is proposed wherein intermediates produced by the electroreduction of $CO_2$ assist in the electrocatalytic production of ammonia from NO. Specifically, the *CO and *COOH produced by $CO_2$ reduction, respectively, promote the deoxygenation and hydrogenation steps in the NO reduction pathway (Scheme 2 and Figures S36 and S37). In the presence of $CO_2$ and NO, both molecules first adsorb onto the catalyst surface. The *$CO_2$ is reduced by gaining one electron and one proton to form *COOH, which is further reduced by another electron and proton, losing water to form *CO. The *CO then assists the adjacent *NO in losing an O atom to become *N. Subsequently, the *CO acquires an O atom and is converted back to $CO_2$, completing the $CO_2$-COOH-CO-$CO_2$ cycle that aids the deoxygenation of *NO. The *N then undergoes three subsequent hydrogenation steps. During this process, the *COOH generated from $CO_2$ can assist the stepwise hydrogenation of *N to form $NH_3$, while *COOH loses an H atom and reverts to $CO_2$, completing the $CO_2$-COOH-$CO_2$ cycle that assists in the hydrogenation of *N.

To further verify the mechanism by which $CO_2$ enhances NO reduction to $NH_3$, density functional theory (DFT) calculations were performed using the Cu(111) structure as the computational model. First, the adsorption configurations of NO on the Cu(111) surface were optimized. According to previous literature, NO tends to bind to transition metals via the N-end on catalyst surfaces.[16,75] Therefore, there are three types of NO adsorption on the Cu(111) surface: top-type (Cu-NO), bridge-type ($Cu_2$-NO), and hollow-type ($Cu_3$-NO). The hollow-type can be further divided into two cases, $Cu_{3fcc}$-NO and $Cu_{3hcp}$-NO. Adsorption energy calculations for these four types of NO adsorption on the Cu(111) surface revealed that $Cu_{3fcc}$-NO is the most favorable adsorption type for NO on the Cu(111) surface (Figures 4a, S38, and Table S3). The Bader charge analysis revealed that 0.47 $e^-$ were transferred to the NO molecule at the $Cu_{3fcc}$ site during NO adsorption on the Cu (111) surface, demonstrating the effective activation of NO at the fcc site of the Cu substrate (Figure S39).

Based on this adsorption configuration, Gibbs free energy ($\Delta G$) calculations were performed for the NO electrocatalytic reduction reaction pathway in the presence and absence of $CO_2$ (Figure 4b–f, Figure S40–S44, and Table S4–S7). In the absence of $CO_2$, the deoxygenation process of *NO involves an energy-absorbing step from *N to *NOH (0.115 eV), followed by dehydration to form *N, which significantly limits the rate and selectivity of NO reduction to $NH_3$. However, with the assistance of *CO, *NO can complete the deoxygenation process in one step to form *N, with *CO reverting to *$CO_2$, bypassing the energy-absorbing step of forming *NOH, which is more energetically favorable than the reduction of NO alone.

Furthermore, during the subsequent continuous hydrogenation of *N, the *COOH formed on the Cu surface during the electroreduction of $CO_2$ can act as H-sources to sustain hydrogenation of *N, *NH, and *$NH_2$. Compared to the pathways utilizing *H for hydrogenation, the reaction Gibbs free energy and activation barriers of the *COOH pathway are significantly decreased. The energy barriers of the three hydrogenation processes—corresponding to the *NH, *$NH_2$, and *$NH_3$ formation steps—are reduced to 0.27, 0.41, and 0.38 eV, respectively, as calculated by the climbing image nudged elastic band (CI-NEB) method (Figure 4g–i, Figures S45–S50, and Tables S8–S13). Meanwhile, accompanied by the transition from *COOH to *$CO_2$, the $CO_2$ re-enters the electrocatalytic NO to $NH_3$ conversion cycle, demonstrating unique catalytic properties. Therefore, *COOH can significantly enhance the hydrogenation rate of *N. These theoretical results are consistent with experimental findings, indicating that the enhancement of NO reduction to $NH_3$ by $CO_2$ is mainly due to the intermediates from $CO_2$

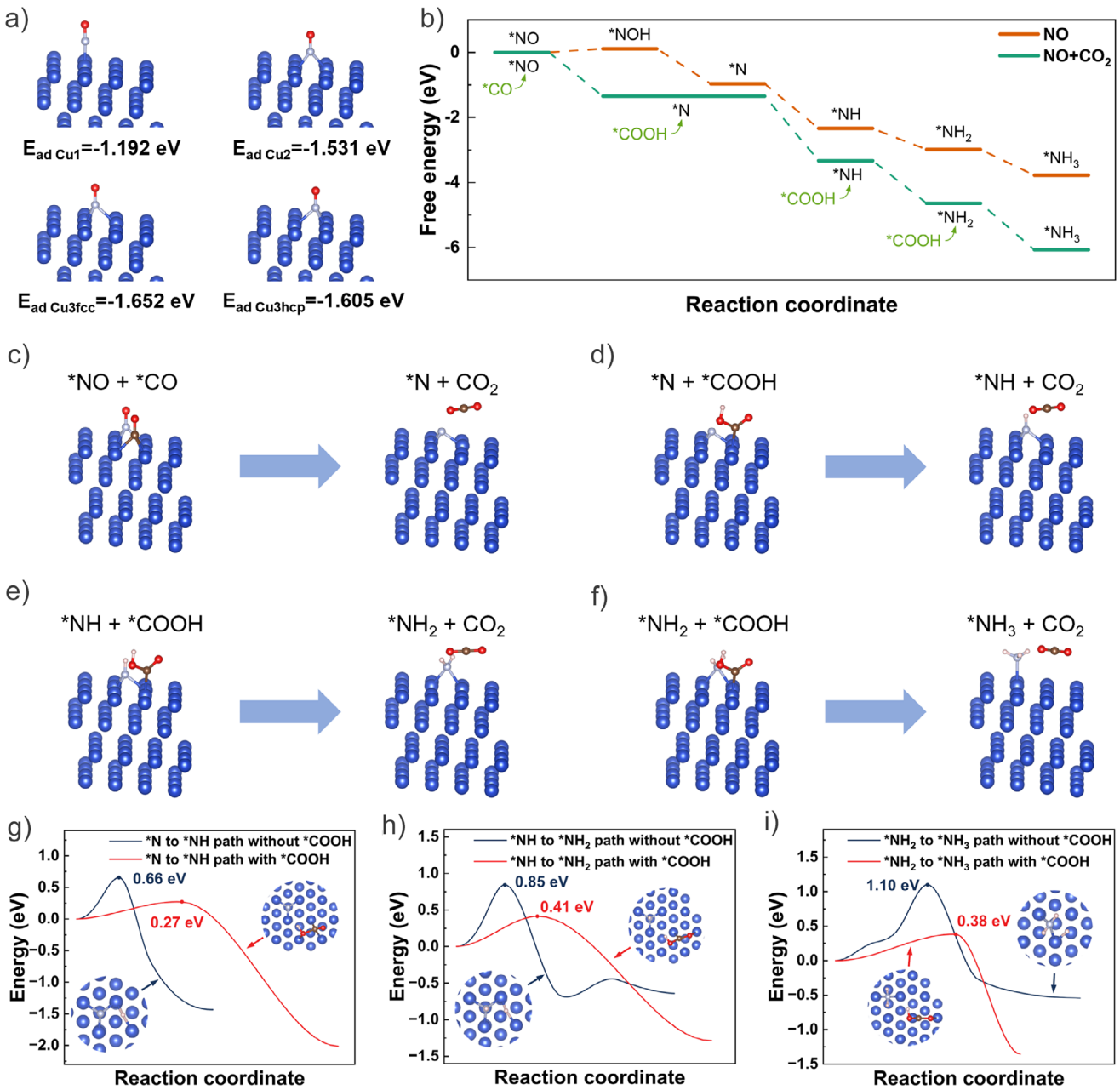


***Figure 4.*** Theoretical calculations of NO reduction with and without $CO_2$. a) Adsorption energy of NO at potential active sites on Cu (111). b) Gibbs free energy diagram for NO reduction to $NH_3$ on Cu(111) with and without $CO_2$. c) *CO-assisted deoxygenation process of *NO. *COOH-assisted hydrogenation process of d) *N, e) *NH, and f) $*NH_2$. Free energy diagrams of g) *N to *NH, h) *NH to $*NH_2$, and i) $*NH_2$ to $*NH_3$ through their respective transition states, with and without *COOH (insets: geometries of the transition states). Cu atoms are labeled in blue, N atoms in gray, O atoms in red, C atoms in brown, and H atoms in light pink.

reduction facilitating the deoxygenation and hydrogenation processes of NO.

## Conclusion

In summary, we have discovered that the presence of $CO_2$ significantly enhances the Faradaic efficiency and yield of the electrocatalytic reduction of NO to $NH_3$. Even under conditions of low concentration NO in simulated flue gas, the strategy demonstrates exceptional $NH_3$ production performance. Experimental and theoretical calculations indicate that *CO and *COOH derived from $CO_2$ promote the deoxygenation of *NO and the hydrogenation of *N at the Cu catalytic interface. This work not only elucidates the impact of actual flue gas components on the electrocatalytic reduction of NO but also provides new insights for enhancing the yield of $NH_3$ from NO recovery. We believe that the strategy of using $CO_2$ to assist in the electrocatalytic reduction of NO to $NH_3$ will attract wide attention for the

removal and resource recovery of NO from industrial flue gases.

## Supporting Information

The authors have cited additional references within the Supporting Information.[76–81]

## Acknowledgements

Y.J. would like to acknowledge the support from the Fundamental Research Funds for the Central Universities-Cemac "GeoX" Interdisciplinary Program and the Frontiers Science Center for Critical Earth Material Cycling of Nanjing University (021114380217, 2024QNXZ07). W.Z. would like to acknowledge the support from the National Natural Science Foundation of China (22176086), the Fundamental Research Funds for the Central Universities (021114380222, 021114380214), the Research Funds for Jiangsu Distinguished Professor, the Carbon Peaking and Carbon Neutrality Technological Innovation Foundation of Jiangsu Province (BE2022861), the Research Funds from the Frontiers Science Center for Critical Earth Material Cycling of Nanjing University, and the State Key Laboratory of Pollution Control and Resource Reuse.

## Conflict of Interests

The authors declare no conflict of interest.

## Data Availability Statement

The data that support the findings of this study are available from the corresponding author upon reasonable request.

**Keywords:** NO electroreduction · $NH_3$ production · Reaction intermediates · Deoxygenation · Hydrogenation

[1] H. D. Shen, C. Choi, J. Masa, X. Li, J. S. Qiu, Y. Jung, Z. Y. Sun, *Chem* **2021**, *7*, 1708–1754.
[2] D. Wang, Z.-W. Chen, K. Gu, C. Chen, Y. Liu, X. Wei, C. V. Singh, S. Wang, *J. Am. Chem. Soc.* **2023**, *145*, 6899–6904.
[3] W. He, J. Zhang, S. Dieckhoefer, S. Varhade, A. C. Brix, A. Lielpetere, S. Seisel, J. R. C. Junqueira, W. Schuhmann, *Nat. Commun.* **2022**, *13*, 1129.
[4] D. Dhanabal, Y. Y. Song, S. Jang, S. Shanmugam, *Appl. Catal. B-Environ. Energy* **2025**, *361*, 124577.
[5] V. Kyriakou, I. Garagounis, A. Vourros, E. Vasileiou, M. Stoukides, *Joule* **2020**, *4*, 142–158.
[6] K. Chu, B. Weng, Z. Lu, Y. Ding, W. Zhang, R. Tan, Y.-M. Zheng, N. Han, *Adv. Sci.* **2025**, *12*, 2416053.
[7] J.-Y. Fang, Q.-Z. Zheng, Y.-Y. Lou, K.-M. Zhao, S.-N. Hu, G. Li, O. Akdim, X.-Y. Huang, S.-G. Sun, *Nat. Commun.* **2022**, *13*, 7899.
[8] IEA, "Ammonia Technology Roadmap", https://www.iea.org/reports/ammonia-technology-roadmap, **2021** (accessed: October 2021).
[9] L. Li, Y. L. Li, K. Li, W. T. Zou, H. H. Li, Y. Li, L. Y. Li, Q. Y. Zhang, C. Y. Zhang, X. F. Zhang, D. L. Tian, L. Jiang, *ACS Nano* **2025**, *19*, 1080–1089.
[10] Y. Ren, S. Li, C. Yu, Y. Zheng, C. Wang, B. Qian, L. Wang, W. Fang, Y. Sun, J. Qiu, *J. Am. Chem. Soc.* **2024**, *146*, 6409–6421.
[11] Y. Pang, C. Su, G. Jia, L. Xu, Z. Shao, *Chem. Soc. Rev.* **2021**, *50*, 12744–12787.
[12] Y. Fu, S. Wang, Y. Wang, P. Wei, J. Shao, T. Liu, G. Wang, X. Bao, *Angew. Chem. Int. Edit.* **2023**, *62*, e202303327.
[13] G. Zhang, X. Li, K. Chen, Y. Guo, D. Ma, K. Chu, *Angew. Chem. Int. Edit.* **2023**, *62*, e202300054.
[14] X. Li, P. Shen, Y. Luo, Y. Li, Y. Guo, H. Zhang, K. Chu, *Angew. Chem. Int. Ed.* **2022**, *61*, e202205923.
[15] Q. Fang, S. Fan, X. Li, D. Zhang, *ACS Appl. Nano Mater.* **2025**, *8*, 1806–1815.
[16] J. Long, S. Chen, Y. Zhang, C. Guo, X. Fu, D. Deng, J. Xiao, *Angew. Chem. Int. Ed.* **2020**, *59*, 9711–9718.
[17] X. Guo, T. Wu, H. Li, L. Chai, M. Liu, *Angew. Chem. Int. Ed.* **2025**, *64*, e202420346.
[18] Q. Yan, J. Xiao, R. Gui, Z. Chen, Y. Li, T. Zhu, Q. Wang, Y. Xin, *Environ. Sci. Technol.* **2023**, *57*, 20708–20717.
[19] G. He, M. Gao, Y. Peng, Y. Yu, W. Shan, H. He, *Environ. Sci. Technol.* **2021**, *55*, 6995–7003.
[20] K. Guo, J. Ji, W. Song, J. Sun, C. Tang, L. Dong, *Appl. Catal. B-Environ.* **2021**, *297*, 120388.
[21] M. Li, M. Gao, G. He, Y. Yu, H. He, *Environ. Sci. Technol.* **2023**, *57*, 3875–3882.
[22] J. Liang, P. Liu, Q. Li, T. Li, L. Yue, Y. Luo, Q. Liu, N. Li, B. Tang, A. A. Alshehri, I. Shakir, P. O. Agboola, C. Sun, X. Sun, *Angew. Chem. Int. Ed.* **2022**, *61*, e202202087.
[23] L. Zhang, J. Liang, Y. Wang, T. Mou, Y. Lin, L. Yue, T. Li, Q. Liu, Y. Luo, N. Li, B. Tang, Y. Liu, S. Gao, A. A. Alshehri, X. Guo, D. Ma, X. Sun, *Angew. Chem. Int. Ed.* **2021**, *60*, 25263–25268.
[24] L. Han, S. Cai, M. Gao, J.-y. Hasegawa, P. Wang, J. Zhang, L. Shi, D. Zhang, *Chem. Rev.* **2019**, *119*, 10916–10976.
[25] Y. Li, C. Cheng, S. Han, Y. Huang, X. Du, B. Zhang, Y. Yu, *ACS Energy Lett.* **2022**, *7*, 1187–1194.
[26] C. Bai, S. Fan, X. Li, Z. Niu, J. Wang, Z. Liu, D. Zhang, *Adv. Funct. Mater.* **2022**, *32*, 2205569.
[27] D. Wang, X. Zhu, X. Tu, X. Zhang, C. Chen, X. Wei, Y. Li, S. Wang, *Adv. Mater.* **2023**, *35*, 2304646.
[28] Z. Wu, Y. J. Liu, D. D. Wang, Y. Q. Zhang, K. Z. Gu, Z. J. He, L. M. Liu, H. W. Liu, J. C. Fan, C. Chen, S. Y. Wang, *Adv. Mater.* **2024**, *36*, 2309470.
[29] J. Shao, H. Jing, P. Wei, X. Fu, L. Pang, Y. Song, K. Ye, M. Li, L. Jiang, J. Ma, R. Li, R. Si, Z. Peng, G. Wang, J. Xiao, *Nat. Energy* **2023**, *8*, 1273–1283.
[30] K. Chen, J. Xiang, Y. Guo, X. Liu, X. Li, K. Chu, *Nano Lett.* **2024**, *24*, 541–548.
[31] B. H. Ko, B. Hasa, H. Shin, Y. Zhao, F. Jiao, *J. Am. Chem. Soc.* **2022**, *144*, 1258–1266.
[32] C. Choi, S. Kwon, Y. Z. Gao, S. Cheon, J. Li, F. Menges, W. A. Goddard, Jr., H. L. Wang, *J. Am. Chem. Soc.* **2024**, *146*, 8486–8491.
[33] Y. Zhang, Y. Wang, L. Han, S. Wang, T. Cui, Y. Yan, M. Xu, H. Duan, Y. Kuang, X. Sun, *Angew. Chem. Int. Ed.* **2023**, *62*, e202213711.
[34] L. Fan, X. Bai, C. Xia, X. Zhang, X. Zhao, Y. Xia, Z.-Y. Wu, Y. Lu, Y. Liu, H. Wang, *Nat. Commun.* **2022**, *13*, 2668.
[35] D. Kim, D. Shin, J. Heo, H. Lim, J.-A. Lim, H. M. Jeong, B.-S. Kim, I. Heo, I. Oh, B. Lee, M. Sharma, H. Lim, H. Kim, Y. Kwon, *ACS Energy Lett.* **2020**, *5*, 3647–3656.

[36] H. Zhang, Y. Li, C. Cheng, J. Zhou, P. Yin, H. Wu, Z. Liang, J. Zhang, Q. Yun, A.-L. Wang, L. Zhu, B. Zhang, W. Cao, X. Meng, J. Xia, Y. Yu, Q. Lu, *Angew. Chem. Int. Ed.* **2023**, *62*, e202213351.
[37] Y. Xiong, Y. Li, S. Wan, Y. Yu, S. Zhang, Q. Zhong, *J. Hazard. Mater.* **2022**, *430*, 128451.
[38] J. Shi, C. Wang, R. Yang, F. Chen, N. Meng, Y. Yu, B. Zhang, *Sci. China-Chem.* **2021**, *64*, 1493–1497.
[39] R. Hao, L. Tian, C. Wang, L. Wang, Y. Liu, G. Wang, W. Li, G. A. Ozin, *Catalysis* **2022**, *2*, 622–638.
[40] H. Wan, A. Bagger, J. Rossmeisl, *Angew. Chem. Int. Ed.* **2021**, *60*, 21966–21972.
[41] A. Bagger, W. Ju, A. S. Varela, P. Strasser, J. Rossmeisl, *ChemPhysChem* **2017**, *18*, 3266–3273.
[42] W. Quan, Y. Lin, Y. Luo, Y. Huang, *Adv. Sci.* **2021**, *8*, 2101597.
[43] Y. Zhao, X. Chang, A. S. Malkani, X. Yang, L. Thompson, F. Jiao, B. Xu, *J. Am. Chem. Soc.* **2020**, *142*, 9735–9743.
[44] H. Du, L.-X. Liu, P. Li, Q. Min, S. Guo, W. Zhu, *ACS Nano* **2023**, *17*, 8663–8670.
[45] H. Du, J. Fu, L.-X. Liu, S. Ding, Z. Lyu, X. Jin, F. O. Kengara, B. Song, Q. Min, J.-J. Zhu, D. Du, C. Gu, Y. Lin, J.-S. Hu, W. Zhu, *Mater. Today* **2022**, *59*, 182–199.
[46] Y. Yang, S. Louisia, S. Yu, J. Jin, I. Roh, C. Chen, M. V. Fonseca Guzman, J. Feijoo, P.-C. Chen, H. Wang, C. J. Pollock, X. Huang, Y.-T. Shao, C. Wang, D. A. Muller, H. D. Abruna, P. Yang, *Nature* **2023**, *614*, 262–269.
[47] L. Xiao, S. Mou, W. Dai, W. Yang, Q. Cheng, S. Liu, F. Dong, *Angew. Chem. Int. Ed.* **2024**, *63*, e202319135.
[48] Z.-Z. Wu, X.-L. Zhang, Z.-Z. Niu, F.-Y. Gao, P.-P. Yang, L.-P. Chi, L. Shi, W.-S. Wei, R. Liu, Z. Chen, S. Hu, X. Zheng, M.-R. Gao, *J. Am. Chem. Soc.* **2022**, *144*, 259–269.
[49] D.-F. Zhang, H. Zhang, L. Guo, K. Zheng, X.-D. Han, Z. Zhang, *J. Mater. Chem.* **2009**, *19*, 5220–5225.
[50] J. Zhou, S. H. Han, R. Yang, T. L. Li, W. B. Li, Y. T. Wang, Y. F. Yu, B. Zhang, *Angew. Chem. Int. Ed.* **2023**.
[51] Y. Huang, R. Yang, C. Wang, N. Meng, Y. Shi, Y. Yu, B. Zhang, *ACS Energy Lett.* **2022**, *7*, 284–291.
[52] Y. R. Shi, H. H. Yi, F. Y. Gao, S. Z. Zhao, Z. L. Xie, X. L. Tang, *Sep. Purif. Technol.* **2021**, *265*, 118517.
[53] Y. R. Shi, H. H. Yi, F. Y. Gao, S. Z. Zhao, Z. L. Xie, X. L. Tang, *J. Hazard. Mater.* **2021**, *413*, 125361.
[54] X. Guo, P. Wang, T. Wu, Z. Wang, J. Li, K. Liu, J. Fu, M. Liu, J. Wu, Z. Lin, L. Chai, Z. Bian, H. Li, M. Liu, *Angew. Chem. Int. Ed.* **2024**, *63*, e202318792.
[55] M. Dunwell, Q. Lu, J. M. Heyes, J. Rosen, J. G. G. Chen, Y. S. Yan, F. Jiao, B. J. Xu, *J. Am. Chem. Soc.* **2017**, *139*, 3774–3783.
[56] P. Mondol, D. Panthi, A. J. A. Ayala, S. O. Odoh, C. J. Barile, *J. Mater. Chem. A* **2022**, *10*, 22428–22436.
[57] J. Qin, N. Liu, L. Chen, K. Wu, Q. Zhao, B. Liu, Z. Ye, *ACS Sustainable Chem. Eng.* **2022**, *10*, 15869–15875.
[58] Z. Niu, S. Fan, X. Li, J. Duan, A. Chen, *Appl. Catal. B-Environ.* **2023**, *322*, 122090.
[59] R. Zhao, Q. Yan, L. Yu, T. Yan, X. Zhu, Z. Zhao, L. Liu, J. Xi, *Adv. Mater.* **2023**, *35*, 2306633.
[60] C. M. Gunathunge, J. Y. Li, X. Li, J. L. J. Hong, M. M. Waegele, *ACS Catal.* **2020**, *10*, 6908–6923.
[61] Y. Bai, S. Gao, Y. Sun, W. Ouyang, Y. Zhou, H. Wang, Z. Wu, *Environ. Sci. Technol.* **2023**, *57*, 9105–9114.
[62] Y. Bai, C. Miao, H. Wang, Z. Wu, *Environ. Sci. Technol.* **2024**, *58*, 11812–11821.
[63] R. Gui, J. Xiao, Y. Gao, Y. Li, T. Zhu, Q. Wang, *Appl. Catal. B-Environ.* **2022**, *306*, 121104.
[64] K. Chen, F. Z. Wang, X. B. Lu, Y. H. Li, K. Chu, *ACS Catal.* **2023**, *13*, 9550–9557.
[65] K. Chen, Y. Zhang, J. Xiang, X. Zhao, X. Li, K. Chu, *ACS Energy Lett.* **2023**, *8*, 1281–1288.
[66] R. Q. Long, R. T. Yang, *J. Catal.* **2000**, *190*, 22–31.
[67] Z. Liu, Y. Lu, L. Yuan, L. Ma, L. Zheng, J. Zhang, T. Hu, *Appl. Catal. B-Environ.* **2016**, *188*, 189–197.
[68] G. Ramis, L. Yi, G. Busca, *Catal. Today* **1996**, *28*, 373–380.
[69] Q. Wang, X. Yang, H. Zang, F. Chen, C. Wang, N. Yu, B. Geng, *Inorg. Chem.* **2022**, *61*, 12003–12011.
[70] X. Yang, Q. Wang, F. Chen, H. Zang, C. Liu, N. Yu, B. Geng, *Nano Res.* **2023**, *16*, 7974–7981.
[71] S. Jin, Z. Hao, K. Zhang, Z. Yan, J. Chen, *Angew. Chem. Int. Ed.* **2021**, *60*, 20627–20648.
[72] S. Zhu, B. Jiang, W.-B. Cai, M. Shao, *J. Am. Chem. Soc.* **2017**, *139*, 15664–15667.
[73] C. Guo, W. Zhou, X. Lan, Y. Wang, T. Li, S. Han, Y. Yu, B. Zhang, *J. Am. Chem. Soc.* **2022**, *144*, 16006–16011.
[74] B. Sun, Z. Li, D. Xiao, H. Liu, K. Song, Z. Wang, Y. Liu, Z. Zheng, P. Wang, Y. Dai, B. Huang, A. Thomas, H. Cheng, *Angew. Chem. Int. Ed.* **2024**, *63*, e202318874.
[75] A. Shiotari, H. Koshida, H. Okuyama, *Surf. Sci. Rep.* **2021**, *76*, 100500.
[76] J. P. Perdew, K. Burke, M. Ernzerhof, *Phys. Rev. Lett.* **1996**, *77*, 3865–3868.
[77] S. Grimme, J. Antony, S. Ehrlich, H. Krieg, *J. Chem. Phys.* **2010**, *132*, 154104.
[78] V. Wang, N. Xu, J.-C. Liu, G. Tang, W.-T. Geng, *Comput. Phys. Commun.* **2021**, *267*, 108033.
[79] G. Henkelman, B. P. Uberuaga, H. Jónsson, *J. Chem. Phys.* **2000**, *113*, 9901–9904.
[80] J. Kaestner, P. Sherwood, *J. Chem. Phys.* **2008**, *128*, 014106.
[81] W. Z. Wang, G. H. Wang, X. S. Wang, Y. J. Zhan, Y. K. Liu, C. L. Zheng, *Adv. Mater.* **2002**, *14*, 67–69.

Manuscript received: February 24, 2025
Revised manuscript received: March 26, 2025
Accepted manuscript online: April 07, 2025
Version of record online: April 17, 2025